Journal of Structural Geology 36 (2012) 43–54

Contents lists available at SciVerse ScienceDirect

Journal of Structural Geology

journal homepage: www.elsevier.com/locate/jsg

Timing and mechanism of late-Pleistocene calcite vein formation across the Dead Sea Fault Zone, northern Israel

Perach Nuriel [a,*], Ram Weinberger [b], Gideon Rosenbaum [a], Suzanne D. Golding [a], Jian-xin Zhao [a,c], I. Tonguc Uysal [a,d], Miryam Bar-Matthews [b], Michael R. Gross [e]

[a] School of Earth Sciences, The University of Queensland, Steele Building, Brisbane, QLD 4072, Australia
[b] Geological Survey of Israel, 30 Malkhe Israel St., Jerusalem 95501, Israel
[c] Radiogenic Isotope Laboratory, CMM, The University of Queensland, QLD 4072, Australia
[d] Queensland Geothermal Energy Centre, The University of Queensland, QLD 4072, Australia
[e] Shell International Exploration & Production Inc., Houston, TX 77025, USA

ARTICLE INFO

Article history:
Received 4 May 2011
Received in revised form
8 December 2011
Accepted 26 December 2011
Available online 30 December 2011

Keywords:
Calcite veins
U–Th dating
Oxygen isotopes
Carbon isotopes
Dead Sea Fault

ABSTRACT

The emplacement of calcite-filled veins perpendicular to the Dead Sea Fault Zone in northern Israel reflects strain partitioning during transpression. We present structural, geochemical, and U–Th geochronological data that constrain the mechanism, conditions and timing of vein formation. Vein walls are strongly brecciated and commonly cemented with coarsely crystalline calcite, whereas calcite-filled veins are composed of wall-parallel bands of calcite crystals. Elongated blocky and fibrous calcite crystals grew perpendicular to the vein walls and are characterised by a truncate sealing-hiatus morphology, indicating episodes of partial or complete sealing of the fractures during calcite precipitation. Stable isotope and rare-earth element and yttrium (REY) analyses indicate that calcite-filled veins precipitated by karst processes, involving meteoric water and limited fluid-rock interactions. U–Th dating results show a prolonged history of vein growth. While some veins initiated prior to 500 ka, the majority of the veins were active between 358 and 17 ka. Age constraints on vein activity correspond to an ~E–W regional shortening phase in this sector of the Dead Sea Fault Zone, associated with an increased component of convergence during the late-Pleistocene.

1. Introduction

Opening-mode fractures are common features in the upper crust, forming perpendicular to the direction of least compressive stresses as a result of brittle or semi-brittle failure (e.g. Hancock, 1985; Bourne and Willemse, 2001). Their formation is commonly associated with fluid circulation and precipitation of vein-fill material (Sibson, 1987; Cox, 2007; Faleiros et al., 2007), giving rise to the formation of dilation veins. The temporal relationship between faulting and formation of dilation veins was studied in numerous tectonic settings (e.g. Peacock, 2001), among which are strike-slip settings, where dilation veins are oriented preferentially in dilational step-overs (jogs) between en-echelon segments (Sibson, 1985; De Paola et al., 2008). The sites of contractional or extensional deformation within step-overs may migrate through time, and the evolution of the step-over can be traced by mineralization along fractures (e.g. Berger, 2007; Eichhubl et al., 2009). Dilation veins may also develop within convergent strike-slip settings in response to perpendicular contraction, reflecting strain partitioning during transpression (Gross and Engelder, 1995; Gross et al. 1997; Swanson, 2006). The study of dilation veins forming within long-lived strike-slip settings may therefore help to detect the spatial and temporal transition in the style of deformation.

The formation of opening-mode fractures can be dynamic, i.e., driven by seismic events, or passive, i.e., driven by a long-term tectonic loading. While the former is commonly associated with fault-related veins, there are relatively few examples where passive fracturing is linked in time to deformation events. In dynamic fracturing, dilation is episodic (Ramsay, 1980; Bons, 2001; Hilgers and Urai, 2002) and fluids are commonly mobilized during the seismic cycle (Fisher et al., 1995; Sample, 2010; Uysal et al., 2009, 2011). Thus, precipitation processes can be temporally linked to the seismic event (Boles et al., 2004; Boullier et al., 2004; Uysal et al., 2007). During passive fracturing, dilation may occur episodically but the fluids are commonly of meteoric origin (Verhaert et al., 2003, 2004; Janssen et al., 2005, 2007) and precipitation of minerals occurs over a relatively long period of time (>100 yrs).

* Corresponding author. Tel.: +61 7 3365 2130; fax: +61 7 3365 1277.
E-mail addresses: p.nuriel@uq.edu.au, pnuriel@hotmail.com (P. Nuriel).

0191-8141/$ – see front matter © 2011 Elsevier Ltd. All rights reserved.
doi:10.1016/j.jsg.2011.12.010

Thus, the temporal relation between fracturing and precipitation processes needs to be demonstrated in order to constrain the timing and duration of the deformation event. In this paper, we integrate microstructural, stable isotope, trace elements, and U–Th geochronological data to constrain the mechanism and timing of vein formation in a convergent strike-slip setting.

The Dead Sea Fault Zone (DSFZ) in northern Israel provides an ideal location to study vein formation in a tectonically active strike-slip setting (Fig. 1). The study area is located in the Kefar Giladi quarry, where numerous calcite-filled veins are exposed perpendicular to a branch of the DSFZ (Fig. 1). Weinberger et al. (2009) showed that during the Pleistocene, the deformation along this sector of DSFZ was partitioned into strike-slip and contractional domains. This study aims to constrain the timing of vein formation within the context of increasing contractional strain during the late-Pleistocene. We evaluate (1) the origin of the associated fluids and precipitation conditions of calcite vein-fill; (2) vein formation and growth mechanism and (3) the timing of dilation and precipitation of calcite vein-fills. We show that the formation of the studied dilation veins provides insights into the spatial and temporal variations of the strain field within the deformed blocks and highlights the complexity of evolving deformation along transform plate boundaries.

2. Geological setting

The DSFZ is a >1000 km long transform boundary accommodating the relative motion between the African (Sinai) and Arabian plates (Garfunkel, 1981); (Fig. 1a). Striking approximately N–S, the fault links the divergent boundary of the Red Sea with the convergent zone of the Taurus-Zagros mountains (Hempton, 1987). Several basins and ranges form prominent structures along its length, including the low topography of the Dead Sea and Hula basins, and the high topography of the Lebanon and anti-Lebanon

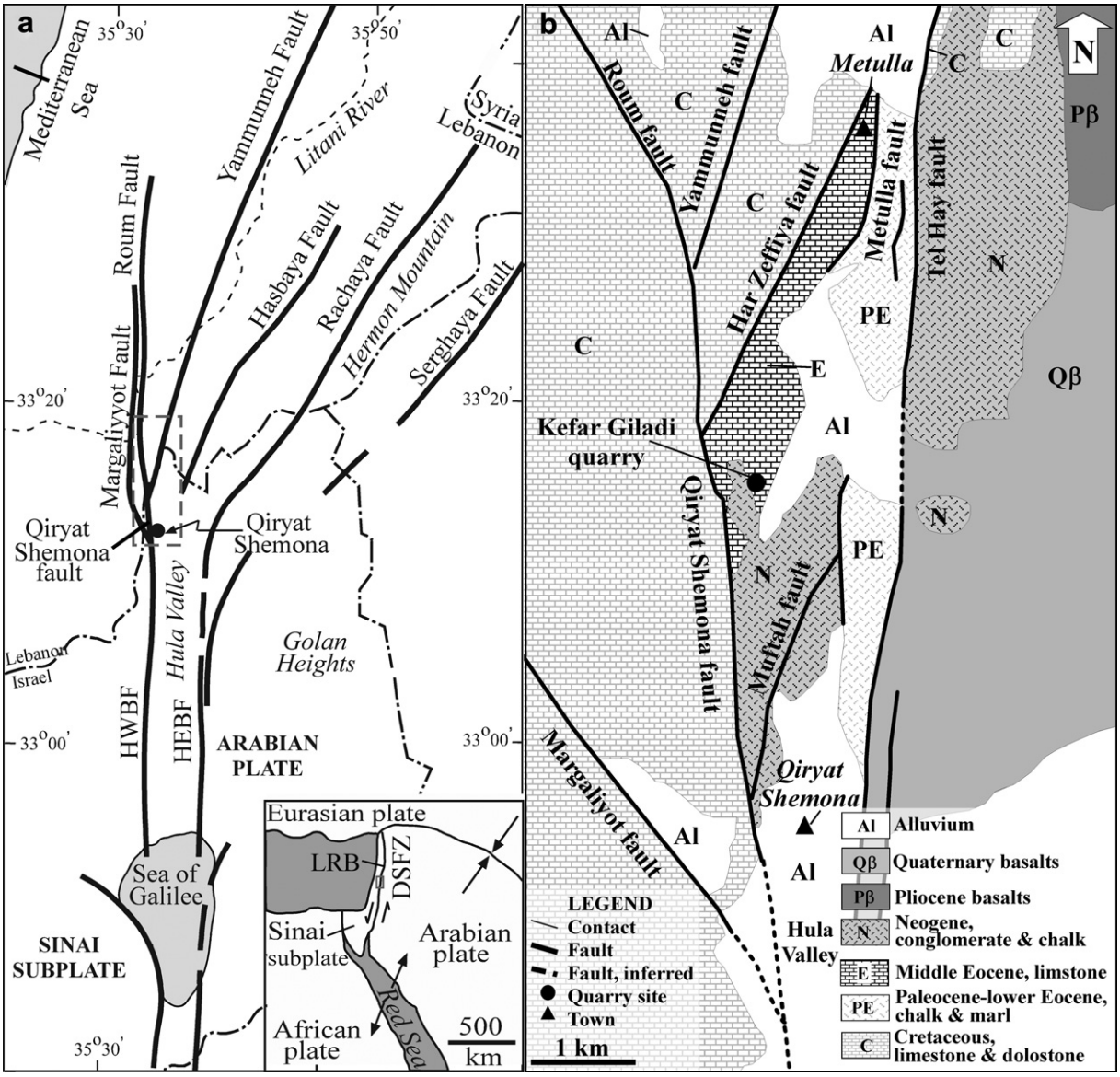

Fig. 1. Tectonic setting of the central sector of the Dead Sea Fault Zone (DSFZ). (a) map of the main segments of the DSFZ in northern Israel and Southern Lebanon (Sneh and Weinberger, 2003; Weinberger et al., 2009); HWBF and HEBF – Hula western and eastern border faults, respectively. The inset shows the plate tectonic configuration resulting in left-lateral motion across the DSFZ (LRB – Lebanon Restraining Band); rectangle shows the location of Fig. 1b; (b) Geological map of the study area showing rock units, faults and location of the Kefar Giladi quarry, 250–500 m to the east of the Qiryat Shemona Fault (modified after Levi and Weinberger, 2011).

ranges in the central sector of the DSFZ (Fig. 1a). Left-lateral movement along the DSFZ commenced within the last ~20 Ma (Eyal et al., 1981; Steinitz and Bartov, 1991), resulting in a total offset of ~105 km (Quennell, 1958; Freund et al., 1968; Garfunkel, 1981; Joffe and Garfunkel, 1987). The relative plate motion is roughly parallel to the N–S trending central sector of the DSFZ, with estimated slip rates of 3–10 mm/yr (Garfunkel, 1981; Joffe and Garfunkel, 1987; Niemi et al., 2001; Meghraoui et al., 2003).

In northern Israel, the main strand of the DSFZ branches into an array of five main transcurrent faults (Fig. 1a). The ~N–S trending Qiryat Shemona Fault (Fig. 1b) is considered the master segment of the DSFZ in the study area (Sneh and Weinberger, 2003). The fault juxtaposes the Eocene Bar Kokhba (limestone; E in Fig. 1b) and Neogene Kefar Giladi Formations (conglomerate and chalk; N Fig. 1b) on the east against the Albian-Cenomanian Judea Group to the west (limestone and dolostone; C in Fig. 1b). It is associated with a wide zone of brittle deformation, including numerous faults and calcite-filled veins, which can be observed at the Kefar Giladi quarry.

Weinberger et al. (2009) have recognised two major directions of regional shortening in the study area: (1) NW–SE shortening that resulted in the formation of NE–SW trending folds, in accordance with the left-lateral displacement along the N–S trending strike-slip faults; and (2) ~E–W shortening as indicated by ~N–S trending folds and N–S striking reverse faults. The Pleistocene (~0.9–1.6 Ma) Hazbani Basalt (Heimann, 1990; Mor, 1993), which crops out east of the Qiryat Shemona Fault (Qβ in Fig. 1b), is affected only by N–S folds, whereas Cretaceous to Neogene strata are folded both along NE–SW and N–S structures. Based on these observations, Weinberger et al. (2009) concluded that the NW–SE phase of shortening predated the ~E–W shortening and the latter has been active since ~1 Ma. Deformation has changed from an early (Miocene-Pliocene) phase of pure (or weak divergent) strike-slip motion to a late (Pleistocene) phase of "partitioned" transpression. The latter is characterised by discrete left-lateral motion across weak N–S faults and the development of folds and reverse faults in the intervening blocks.

3. Field observations

Field observations in the Kefar Giladi quarry (Fig. 2a) included the documentation and structural measurements of calcite-filled veins and fault planes. More than 100 subsidiary fault planes are distributed throughout the quarry (Fig. 2b). The surface exposures of individual fault planes are up to 50 m high and 100 m long, and are commonly associated with polished surfaces, fault striations, fault gouge and breccia zones (Fig. 3a). The most abundant set of vertical fault planes strikes ~N–S, whereas a less abundant set of fault planes strikes approximately ~E–W (Fig. 2b). Calcite-filled veins and clastic dykes are found throughout the Kefar Giladi quarry (see supplementary data set 1). The veins are commonly oriented roughly perpendicular to the ~N–S striking fault planes, and occasionally utilize pre-existing fault planes. Crosscutting relations between the fault planes and calcite-filled veins suggest that veins generally post-date the fault structures (Fig. 3b). The mean direction of calcite-filled veins is 284° (86–014; Fig. 2c). Contouring the data suggests that two sets exist: a dominant E–W striking set and a less dominant NW–SE striking set (Fig. 2c). Veins exposed in the quarry is up to 20 m high (Fig. 3b), and their thickness range between 1 and 31 cm, with the majority being less than 10 cm thick (Fig. 2c). No correlation is recognized between vein orientation and thickness (Fig. 2c).

The veins are built up by successive parallel veinlets of calcite bands, ~1–10 mm wide each (Fig. 3c), with no evidence of shearing along calcite vein-fill or between calcite veinlets. Some veins developed from both sides of the vein walls (i.e., calcite growth is from both walls towards the centre), indicating symmetric growth. Most veins, however, appear to have an asymmetric growth texture, associated with growth planes closer to one side of the vein wall (Fig. 3c). The interface between the vein walls and the parallel veinlets is commonly associated with a dilational breccia zone, which consists of fragments of the host rock and calcite cement. Vein-wall fragments, coated with a thin layer of calcite, are occasionally incorporated into the breccia zones, forming complex vein structures (Fig. 3d). Karst-type amorphous and botryoidal calcite morphology was observed along some vein interfaces (Fig. 3e). Several clastic dykes within the uppermost levels of the quarry (<10 m from surface) are filled by clastic material consisting of soil, gravel, silt and pebbles (Fig. 3f). In these fractures, fibrous bands of calcite veins are seldom developed (Fig. 3f).

Bedding of the host-rock limestone (Bar Kokhba Formation) in the study area is mildly folded, forming an anticline with a fold axis plunging 7° to azimuth 217° (Fig. 2d). Based on its trend, this fold is attributed to an early, Miocene-Pliocene, stage of deformation (Weinberger et al., 2009). The best clustering of vein orientations are obtained *in situ*, i.e., with present bedding orientations, whereas unfolding the limbs results in greater scatter. This indicates that folding occurred prior to vein formation.

4. Microstructural observations

We sampled seven key veins out of the 46 studied veins (see supplementary data set 1) and performed a detailed petrographic investigation on oriented thin-sections, including microscopy and cathodoluminescence (CL), aiming at characterising calcite crystal primary texture and growth history. The studied samples are characterised by highly brecciated vein-walls (Fig. 4). Two types of breccia are recognized in the contact zone between the veins and host rock. The first breccia (type-1) is characterised by fitted-fabric texture, in which *in situ* large angular to sub-rounded limestone fragments, with edges that match adjacent fragments, are separated from each other by narrow zones filled with microcrystalline carbonate cement (Fig. 4a–b). In some veins, host-rock fragments of the breccia have sharp cutting edges that are aligned parallel to vein walls (Fig. 4a), indicating that pre-existing (type-1) breccia fragments were sharply cut during vein initiation. The second type of breccia (type-2) is characterised by a higher proportion of cement and much smaller fragments that are displaced from the site of fragmentation (Fig. 4c–g). The cement of the second breccia-type is coarsely crystalline, with grain size up to several mm in diameter, and well-preserved primary growth texture (i.e., growth competition texture; Fig. 4d). The breccia fragments are completely enclosed by the calcite cement (Fig. 4g). In addition, euhedral calcite crystals are facing the remaining cavities (Fig. 4d–e), indicating that dilation outlasted cementation processes.

On the micro-scale, calcite crystals of vein-fill material show elongate-blocky to fibrous texture. Length to width ratio range between 6 and 100 with lengths up to 5 cm (Table 1). Calcite crystals appear to nucleate from microcrystalline carbonate fragments of wall-rock material (Fig. 5a), and crystal fibres are arranged perpendicular to both vein-walls and parallel veinlets (Fig. 5b). Some veins are found to be completely sealed, showing crystal faces that are truncated by the opposing vein wall (Fig. 5c). This vein was also characterised by thin-twinned crystal morphology (Fig. 5c), suggesting post-formation deformation, possibly due to vein sealing. Calcite grain boundaries are commonly non-planar (Fig. 5b), but occasionally have straight grain boundaries and uniform extinction (Fig. 5d). Growth competition texture ('GCT' in Fig. 5a) is observed in the transition from vein walls and depositional hiatuses (Fig. 5f), as indicated by the increase in the size and width of

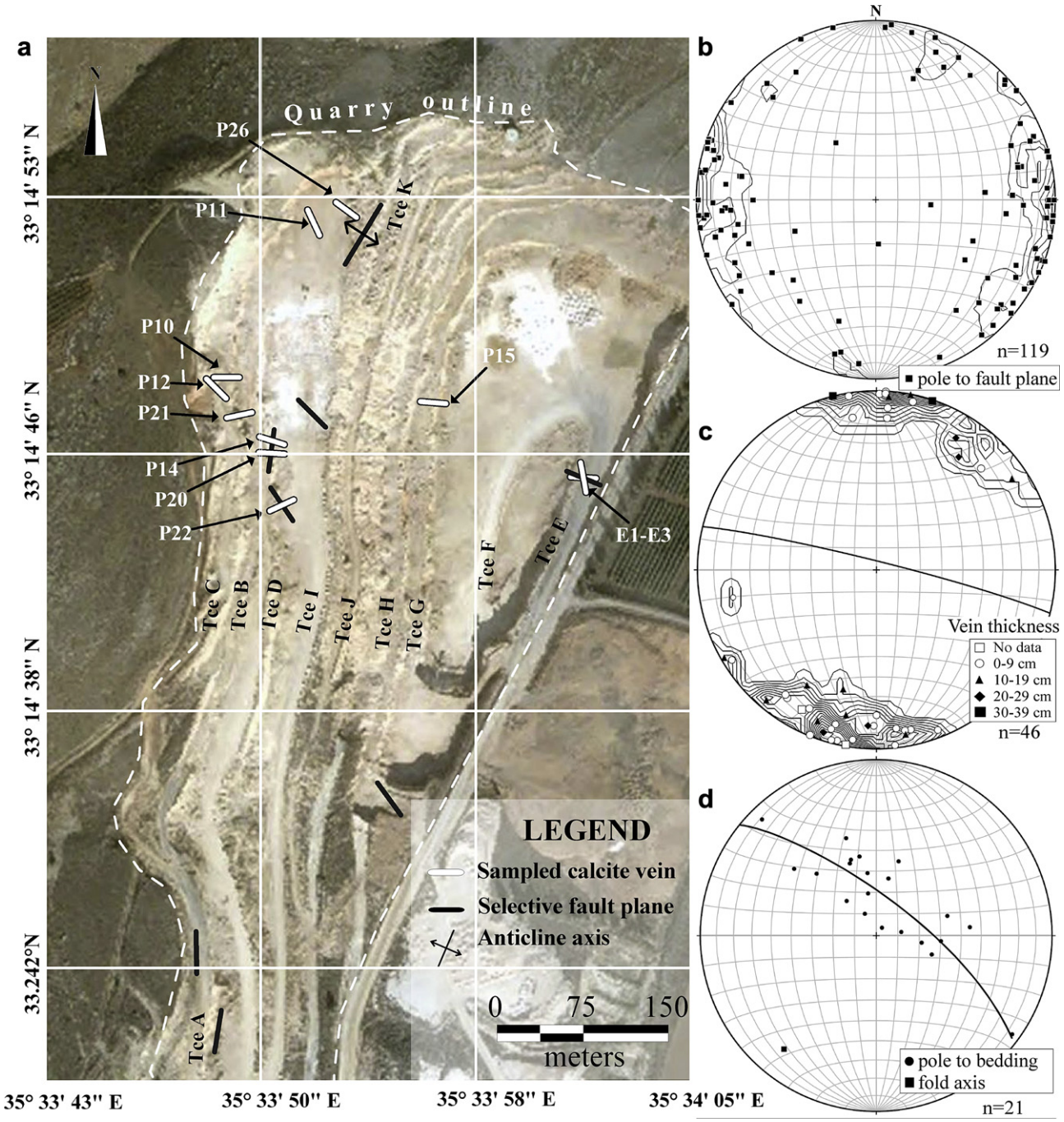

Fig. 2. Structural observations in the Kefar Giladi quarry. (a) Locations and orientations of sampled calcite-filled veins, major fault planes, and anticline axis are shown on the backdrop of an air photo of the Kefar Giladi quarry. Terraces within the quarry (Tce A to K), and calcite vein structures (P10 to P26) are labeled (see also supplementary data set 1); (b) contoured poles to fault planes ($n = 119$) in the Kefar Giladi quarry, showing that most faults are vertical and strike between NNE and NNW directions (from Weinberger et al., 2009); (c) contoured poles to vein planes showing the strike of 46 calcite-filled veins from the Kefar Giladi quarry with mean direction of 284°. Vein data are plotted into groups based on thickness (in cm), showing no clear correlation between vein thickness and orientation; (d) equal Area plot of bedding measurements ($n = 21$), showing a fold axis plunging 07° toward 217° (location of anticline is shown in a).

crystals in the direction of vein growth (arrows in Fig. 5a, c). All veins show growth direction towards the centre of the vein (median plane). Thus the Kefar Giladi veins are classified as syntaxial veins (Durney and Ramsay, 1973). This is also supported by U–Th ages of calcite vein-fill, which show youngest ages at the median plane and oldest at the vein-wall contact (sub-section 6.2).

Calcite depositional hiatuses are common. Three different types of hiatuses were recognized based on their morphology: (1) a sharp truncated crystal termination zone parallel to the vein wall, with steep-sided crystal termination (Fig. 5d, h); (2) euhedral crystal faces termination zone parallel to vein wall (Fig. 5e, g); and (3) a thick hiatus zone marked by a layer of microcrystalline calcite (Fig. 5f). Nucleation of new calcite grains, with visible growth competition texture (Fig. 5g), may have developed following these hiatuses, and in particular where the growth episode terminates with euhedral crystal faces (Fig. 5g). For each vein, all types of

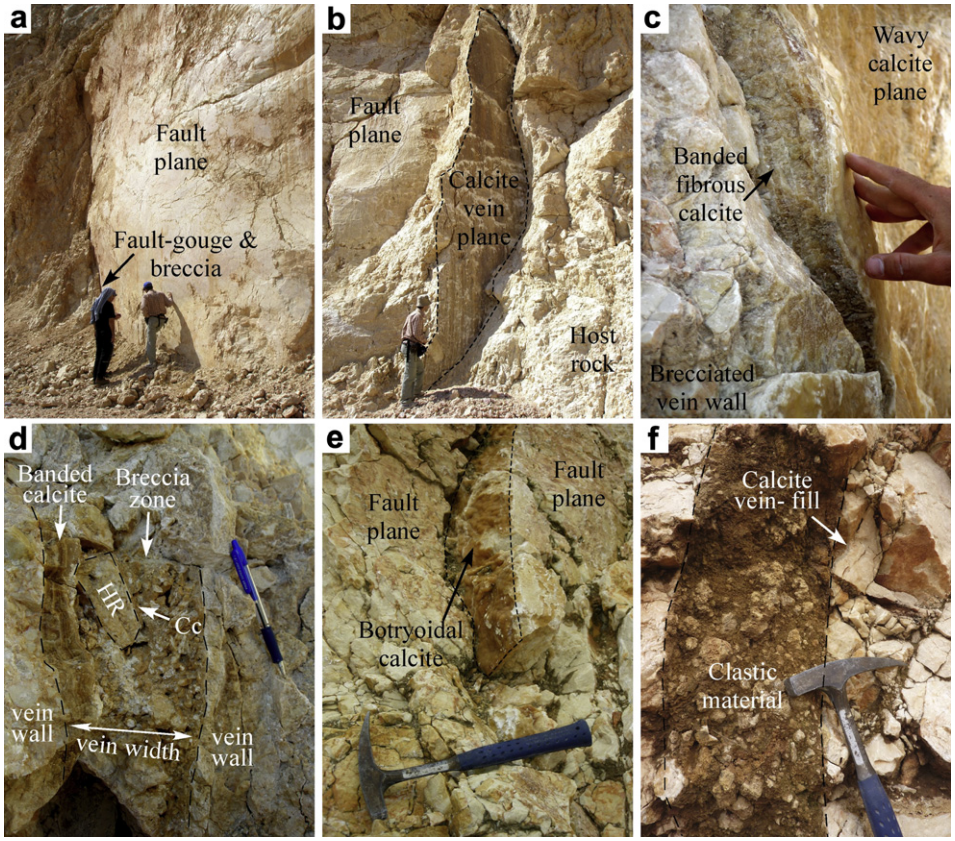

Fig. 3. Fault and vein structures in the Kefar Giladi quarry. (a) ~N–S striking polished vertical fault plane; (b) calcite vein (sample P11) cross-cutting sub-vertical fault plane (top left); (c) asymmetric growth of banded calcite veinlets aligned parallel to wavy vein wall (sample P12); (d) composite 20 cm thick vein with blocks of vein wall fragments ('HR'), with thin calcite coating layer ('Cc'), incorporated into the breccia zone (sample P26); (e) Botryoidal calcite vein utilizing pre-existing fault plane and cross-cutting another sub-vertical fault plane at a right-angle (sample P22); (f) open fracture filled with clastic material and coated with thin calcite layer on vein walls (sample E1).

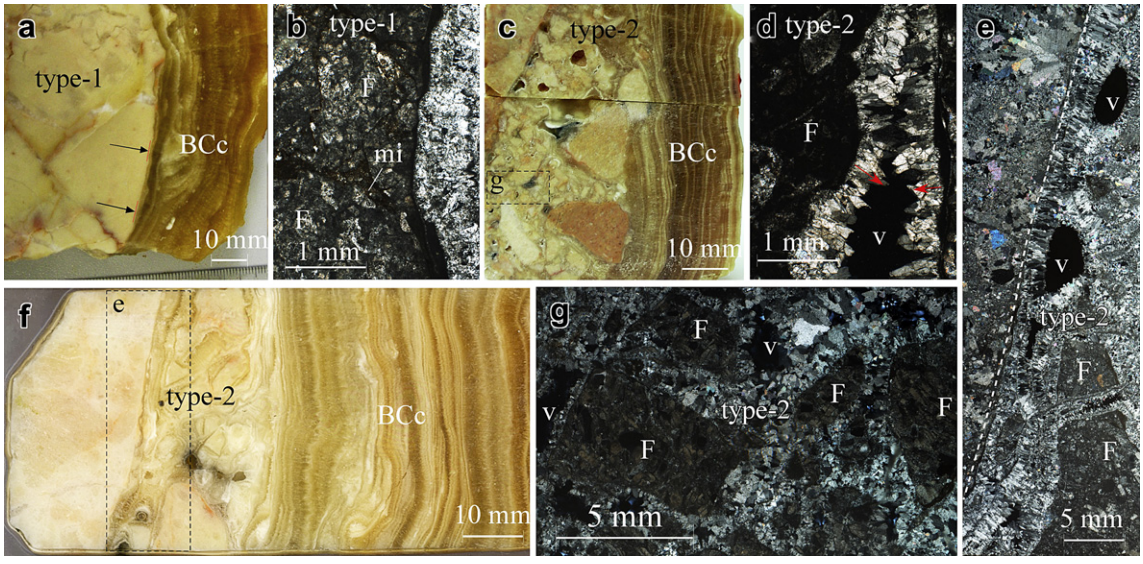

Fig. 4. Vein-wall breccia and transition to banded calcite. (a) sharp transition from vein-wall type-1 breccia to banded calcite (BCc), note the sharp breccia fragment edges aligned parallel to vein wall (marked with arrows; sample P20b); (b) crossed polarized light image of type-1 breccia (sample P20a), showing angular host-rock fragments ('F'), with microcrystalline carbonate cement ('mi'). Note the sharp fragment edges aligned parallel to vein wall; (c) transitions from type-2 breccias to banded calcite (sample P15); (d) coarsely crystalline calcite cement within type-2 breccia (sample P11, crossed polarized light); (e) type-2 breccia showing voids with euhedral crystal faces of the coarsely crystalline calcite cement (sample P11a, crossed polarized light); (f) sharp transition from type-1 breccia to type-2 breccia and to banded calcite (sample P11b); (g) type-2 breccia showing host-rock fragments surrounded completely by the coarsely crystalline calcite cement (sample P15, location is shown in c).

Table 1
U–Th ages, stable isotopes, and microstructural observations of calcite-filled vein samples. Sub-samples names indicate the exact location of the sample within each vein with respect to the distance from the corresponding vein wall. Sub-samples thickness is given in mm. The $\delta^{18}O$ and $\delta^{13}C$ values are with analytical reproducibility better than ±0.1‰ (1σ error). L/W refers to length to width ratio of calcite crystals. Breccia types include: old generation (1) and young generation (2). Hiatus types include: truncated crystal faces (1), or partially truncated crystal faces (2), with a thick micritic layer followed by nucleation and growth competition texture (3).

Vein	Sub-sample (from–to in mm)	Thickness (mm)	U–Th age (ka)	±2σ (ka)	$\delta^{13}C$ ‰V_PDB	$\delta^{18}O$ ‰V_PDB	Crystal size (mm)	L/W ratio	Hiatus/breccia type
P10	P10_2–8	6	358	15	−8.9	−5.3	3	10	3
	P10_25–32	7	53.62	0.46	−9.7	−5.2	5	10	2,3
P11	P11a_Breccia1		>500		−8.9	−6.2	1	3	2
	P11a_Breccia2		>500		−8.8	−6.2	1	3	2
	P11a_15–20	5	305.0	5.4	−8.6	−5.4	2	20	1,2,3
	P11a_30–35	5	129.5	1.2	−9.0	−5.5	15	50	1
	P11b_7–13	6	>500		−7.8	−5.9	2	2	1,2
	P11b_52–58	6	98.38	0.69	−8.8	−5.7	30	100	1,2
P12	P12-Breccia		274.6	5.4	−9.3	−5.4	5	3	2
	P12_7–12	5	236.7	2.3	−10.0	−5.7	5	10	1
	P12-20–23	3	190.9	2.2	−9.3	−6.0	10	30	1,2
	P12-29–32	3	179.8	3.0	−9.2	−5.5	10	10	1,2
	P12-37–40	3	177.1	2.2	−9.4	−8.1	15	30	1,2
	P12_42–47	5	176.8	1.5	−9.2	−6.9	7	10	2
	P12-52–55	3	141.7	1.5	−10.1	−4.9	10	10	1,2
	P12_61–66	5	110.64	0.68	−10.4	−5.6	8	10	1,2
	P12-80–83	3	28.38	0.25	−9.5	−5.2	10	30	1,2
P14	P14-2–8	6	352	6.5	−10.1	−5.7	25	60	1
	P14-15–20	5	350	9.5	−10.0	−6.4	40	100	1,2
	P14-60–70	10	37.75	0.20	−10.3	−5.6	25	60	1,2
P15	P15_4–14	10	154.6	1.0	−9.2	−5.5	7	20	1
	P15_17–22	5	103.58	0.55	−11.7	−6.2	12	20	1
	P15_46–49	3	16.61	0.43	−11.6	−4.8	5	10	1
P20	P20a-1.5–3.5	2	>500		−9.2	−6.2	15	50	1,2
	P20a-15–18	3	261.4	3.6	−10.2	−5.3	10	6	2
	P20a-43–47	4	199.7	2.5	−9.6	−7.0	20	30	1,2
	P20a-62–64	2	34.58	0.61	−8.9	−5.2	20	30	1,2
	P20b-Breccia		>500		−9.9	−6.1	30	1	2
	P20b-0.5–3.5	3	>500		−10.2	−5.2	5	25	2,3
	P20b-10–13	3	278.1	4.5	−9.5	−5.3	12	60	1,2
	P20b-23.5–26.5	3	164.7	2.1	−8.6	−5.1	10	40	1,2
	P20b-32–35	3	24.75	0.43	−8.6	−5.1	10	30	1,2,3
P21	P21-1.5–4.5	3	>500		−8.4	−6.1	3	6	1,2,3
	P21-17–20	3	251.5	4.7	−11.0	−5.6	12	20	1,2
	P21-26–29	3	228.9	4.3	−10.6	−6.2	15	40	1,2
	P21-36.5–39	2.5	25.61	0.53	−10.9	−5.5	15	40	1,2

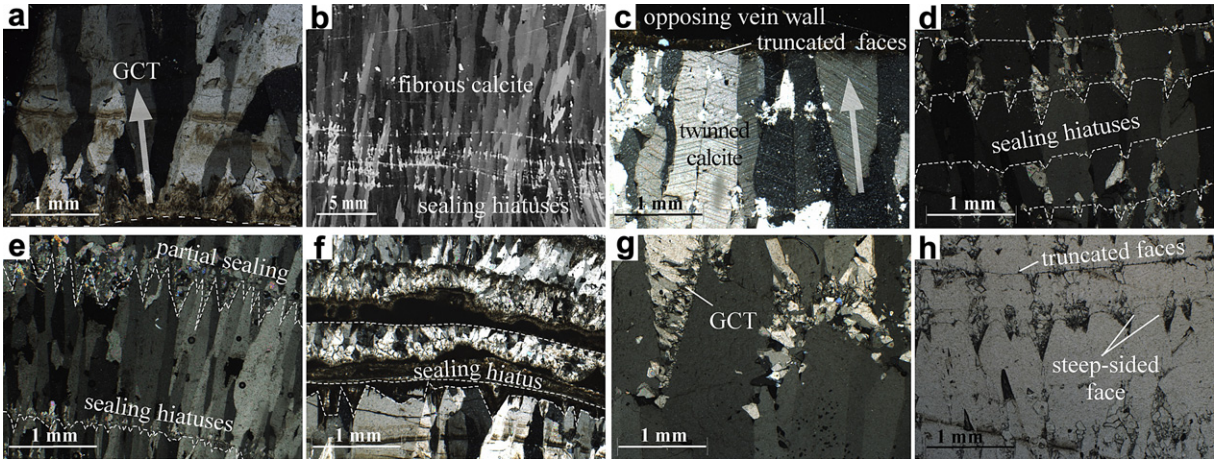

Fig. 5. Photomicrographs of banded calcite-filled veins taken with crossed polarized light. (a) sharp transition from vein wall to calcite vein fill (dash line). Note the nucleation of calcite crystals from microcrystals along vein wall and the growth competition texture (GCT; sample P15). Arrow indicates growth direction; (b) highly elongated (length/width ratios ~100) and up to 4 cm long fibrous crystals (sample P14); (c) truncated crystal faces due to vein sealing (sample P10), with twinned crystal morphology. Arrow indicates growth direction; (d) successive hiatuses in sample P14, locations of truncated termination zone parallel to vein wall are shown with dash lines; Note the straight grain boundaries and close to uniform extinction; (e) successive hiatuses in sample P11a with partial sealing, and euhedral faces termination zone; (f) thick hiatus zone with truncated crystal faces and a layer of microcrystalline carbonate in sample P15; (g) euhedral crystal faces showing nucleation of new calcite grains with growth competition texture (GCT; sample P14); (h) plane polarized light (PPL) image of (d), showing truncated and steep-sided crystal faces.

hiatuses were documented (Table 1) and discussed in sub-section 7.2. Inclusion bands (parallel to the vein– wall) and inclusion trails (subnormal to the vein– wall) (Hilgers and Urai, 2002) which are common features in veins that are built-up by successive incremental opening and filling episodes (Ramsay, 1980), were not identified in the Kefar Giladi veins.

Most vein samples (P11, P12, P14 and P15) were examined under cathodoluminescence (CL) light. Results show no luminescence of calcite vein-fill material and low luminescence of the brecciated host-rock limestone. Additionally, the coarsely crystalline calcite cement facing the remaining cavity shows euhedral crystal faces with no luminescence.

5. Stable isotope and REY geochemistry

5.1. Stable isotope and REY methodology

Three sets of samples were analysed for stable isotopes and rare-earth element + yttrium (REY), (see supplementary data set 2): (1) unaltered host-rock samples taken away from the fault zone (HR-10, HR-11); (2) altered host-rock samples taken from the vein-wall, close to calcite vein-fill interface (marked with HR and associated vein name); (3) calcite vein fill, taken at different distances from the vein-wall within each vein (sub-samples in Table 1). Oxygen and carbon isotope analyses were carried out in the Stable Isotope Geochemistry Lab at The University of Queensland. The extraction of CO_2 was performed on a CO_2 extraction line for the host-rock samples (see Swart et al., 1991 for procedure) and using an on-line multi-prep, microanalysis system for the calcite vein-fill samples. Isotope measurements were obtained on an Isoprime Dual Inlet stable isotope ratio mass spectrometer (SIRMS) that was calibrated using NBS-18, NBS-19, and ANU-M2 carbonate standards. The $\delta^{13}C$ and $\delta^{18}O$ are compared to V-PDB, in per mil ‰ and have an analytical reproducibility better than ±0.1‰ (1σ error).

Under most magmatic and sedimentary conditions, Y behaves almost exactly like its geochemical twin Ho. However, under hydrothermal conditions, Y is known to be fractionated from Ho, resulting in suprachondritic Y/Ho ratios >27 (Bau and Dulski, 1999). We therefore plot the Chondrite-normalized rare-earth element pattern together with yttrium (REY) in order to provide further information on the fluid-flow event leading to calcite precipitation. The REY were analysed on a Thermo X-series ICP-MS instrument with conditions as described in Lawrence and Kamber (2006). Calcite powders were dissolved in a 2% nitric acid solution premixed with internal standards consisting of ^{6}Li, ^{61}Ni, ^{103}Rh, ^{115}In, ^{187}Re, ^{209}Bi and ^{235}U (^{6}Li, ^{61}Ni and ^{235}U are enriched isotopes) for internal correction of mass response drift following the protocol described in Eggins et al. (1997). Apart from internal drift correction, the raw data were also corrected for the low, but detectable blank, isobaric interferences from oxides and doubly charged species. The corrected raw data were then externally corrected for additional drift by repeated measurements of a matrix-matched drift-monitoring solution after the measurement of every 5–7 unknown samples. The raw data were converted into concentrations in ppm using two independent digestions of the USGS reference material W-2 as the calibration standards. The preferred elemental concentration values of W-2 are those reported in Lawrence and Kamber (2006).

5.2. Stable isotope and REY results

Stable isotope values of calcite-filled veins and host-rock limestone are presented in Fig. 6. Oxygen and carbon isotopes values of speleothems from the Peqi'in cave (located 30 km south-west of the Kefar Giladi quarry; Bar-Matthews et al., 2003), are shown in the background of Fig. 6 for comparison purposes. The average $\delta^{13}C$ (V-PDB) and $\delta^{18}O$ (V-PDB) values of calcite-filled veins are −9.6 ± 1.0‰ and −5.7 ± 0.7‰, respectively. The average $\delta^{13}C$ and $\delta^{18}O$ values of the Eocene Bar Kokhba host rock (HR) are −5.8 ± 0.9‰ and −8.6 ± 0.3‰, respectively (see supplementary data set 2). These host rock values correspond to the typical range of marine carbonates with slightly altered values from the primary isotopic signature of the Eocene limestone [i.e., $\delta^{13}C$ between −8‰ and +1‰ and $\delta^{18}O$ between −8‰ and +5‰; (Veizer and Hoefs, 1976)]. Comparing the $\delta^{13}C$ and $\delta^{18}O$ values of calcite-filled veins to their host rocks indicate depletion in the carbon (~4‰) and enrichment in oxygen (~3‰) heavy isotopes in the veins.

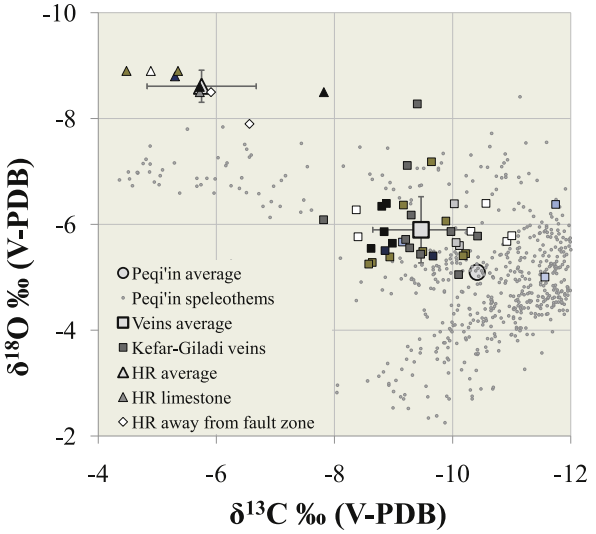

Fig. 6. Stable isotope ($\delta^{18}O$ and $\delta^{13}C$ V-PDB) values of calcite-filled veins (squares) on the backdrop of isotopic values of speleothems from the Peqi'in cave (grey dots; Bar-Matthews et al., 2003). Stable isotope composition of carbonate host-rock samples (Bar Kokhba Formation) taken from the Kefar Giladi quarry (small triangle) are shown with similar colures to corresponding calcite veins. Host-rock values of Bar Kokhba Formation taken away from the fault zone are shown with diamonds. Average values are shown by large symbols.

The REY concentrations of calcite-filled vein samples are considerably lower in comparison with the host rocks, and close to the detection limit of the analytical method (total REY at ~10^{-3} ppm level; see supplementary data set 2). However, the chondrite-normalized REY patterns of the vein samples with relatively higher REY concentrations (e.g. P21 and P20b in Fig. 7) resemble those of the host-rock samples (HR-P21 and HR-P20b, respectively), and both veins and host rock have negative Ce and positive Y anomalies that are typical of carbonates precipitated in a marine environment (Fleet, 1984; Bolhar et al., 2004).

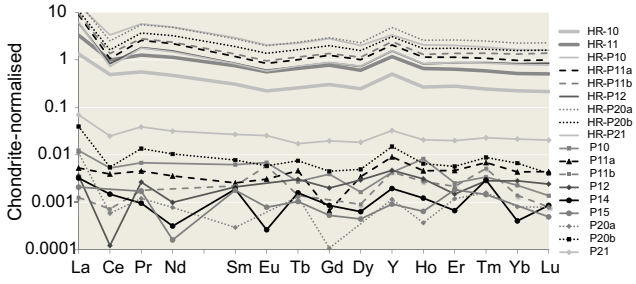

Fig. 7. Chondrite-normalized REY patterns for calcite-filled vein and host-rock samples in the Kefar Giladi quarry. Note the similar REY pattern of vein and host-rock samples (most noticeable in sample P21 and P11a veins), and the low REY composition in all veins relative to their host rocks. Chondrite values are from Haskin et al. (1971).

6. U-series geochronology

6.1. U-series methodology

U-series dating was carried out in the Radiogenic Isotope Laboratory at the University of Queensland following the analytical procedures described in Zhao et al. (2001) and Yu et al. (2006). Calcite samples were separated from calcite bands in each vein at different distances from the vein-wall, and with different thicknesses (sub-sample names in Table 1 refer to the location of band, in mm, from vein wall). In order to avoid contamination with host-rock material, samples were taken at least one mm away from the vein walls. Powdered sub-samples were completely dissolved in concentrated HNO_3 with a mixed ^{229}Th–^{233}U–^{236}U spike. After digestion, U and Th were co-precipitated with iron hydroxide, and then redissolved in nitric acid prior to purification using conventional anion-exchange column chemistry. The U and Th fractions were then loaded onto zone-refined rhenium filaments, sandwiched in between two graphite layers. Isotope ratios were measured in a peak jumping mode on a Daly detector, with Th being measured manually and U automatically on a VG Sector-54 thermal ionization mass spectrometer (TIMS). The $^{230}Th/^{238}U$ and $^{234}U/^{238}U$ activity ratios were calculated using decay constants of Cheng et al. (2000). The non-radiogenic ^{230}Th correction has a minimal impact on the corrected ^{230}Th ages (Richards and Dorale, 2003), as the $^{230}Th/^{232}Th$ activity ratios are commonly higher than 100 in most samples (see supplementary data set 3). U–Th ages were calculated using the Isoplot/Ex Program Version 2 (Ludwig, 1991).

6.2. U-series results

U–Th ages of calcite-filled veins from the Kefar Giladi quarry are presented in Table 1 (additional analytical results are given in supplementary data set 3). The $^{230}Th/^{232}Th$ ratios of all samples are very high (> 100, excluding sub-sample P21_3.65–3.9 with a ratio of 22), implying that non-radiogenic ^{230}Th is negligible. The $^{234}U/^{238}U$ activity ratios of all samples are plotted around the 1.15 ± 0.1 (1σ) evolution line (Fig. 8), implying no significant uranium loss or accumulation during ageing, and therefore confirming closed-system conditions with respect to uranium (Ku, 1965). U–Th ages of calcite breccia cement (P11a and P20b), and sub-samples taken next to vein walls (P11a, P20a, b and P21) are close to the limit of the U–Th method, and their ages may therefore exceed 500 ka. U–Th ages of all other sub-samples range between 358 and 17 ka, with ±2σ errors between 0.2 and 3 ka for samples younger than 200 ka, and between 2.3 and 15 ka for samples older than 200 ka (Table 1).

All U–Th ages are consistent with the vein growth direction as observed in the microstructural study, with ages younging from the vein wall to vein centre (Table 1). The maximum ages of the veins are occur around 360, 280, 260 and 155 ka, and most calcite veins stop their current growth in a time range of ~38 ka up to 17 ka (Fig. 8).

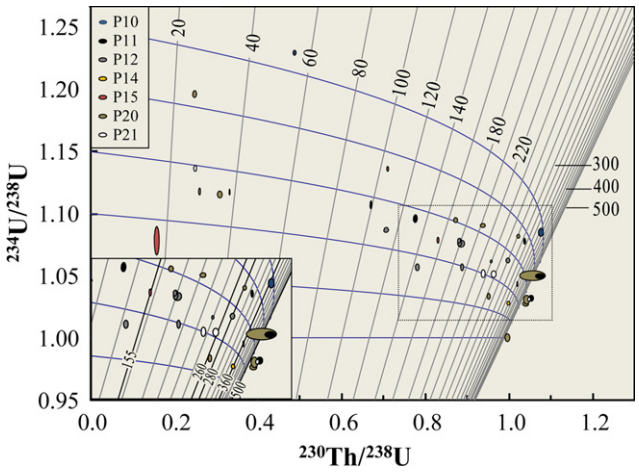

Fig. 8. Plot of activity ratios $^{234}U/^{238}U$ against $^{230}Th/^{238}U$ for calcite vein-fill samples from this study. Data-points are 2σ error ellipses. The U–Th ages (in ka) are shown by sub vertical isochron lines and evolution curves for initial $^{234}U/^{238}U$ ratios are shown by sub horizontal blue lines. Note that $^{234}U/^{238}U$ activity ratios of all samples are plotted around the 1.15 ± 0.1 (1σ) evolution line, implying no significant uranium lost or accumulation subsequent to calcite precipitation. Ages are ranging from > 500 (secular equilibrium), to 17 ka. The majority of the veins initiated during the period between 358 and 155 ka. Black vertical isochron lines in the enlarged inset indicate oldest obtained U–Th ages of calcite vein fill (at > 500, 360, 280, 260, 155 ka). Minimum ages of calcite vein fill are ranging between 38 and 17 ka.

7. Discussion

7.1. Fluid origin and conditions of calcite precipitation

Calcite precipitation may be associated with fluids that have different origins and residence time (e.g. meteoric, host-rock buffered groundwater, mobile deep-seated brines). The geochemistry of the Kefar Giladi calcite-filled veins is indicative for near-surface precipitation by meteoric water with various degrees of fluid-rock interactions. This view is supported by the significant depletion in ^{13}C with respect to the adjacent host rocks, indicating the involvement of H_2O–CO_2 mixed fluids such as meteoric water enriched by C_3-type Mediterranean vegetation (Bar-Matthews et al., 1996).

The stable isotope compositions of the calcite-filled veins are comparable with measured values of oxygen and carbon isotopes in speleothems from the nearby Peqi'in cave (located 30 km southwest of the Kefar Giladi quarry; Bar-Matthews et al., 2003), suggesting precipitation under similar conditions. The $\delta^{18}O$ (V-SMOW) values of palaeo-rainwater in the Eastern Mediterranean during the late-Pleistocene are estimated to range between −3 and −9‰, based on deduced land temperatures in the Soreq cave (Bar-Matthews et al., 2003; McGarry et al., 2004). Using the experimental and theoretical fractionation factors for oxygen isotope in the carbonate system (O'Neil et al., 1969), and the range of $\delta^{18}O$ (V-PDB) of the Kafar Giladi veins (−8.1 to −4.8‰), the temperatures during calcite precipitation are estimated to range between 5 and 30 °C.

The REY patterns of calcite precipitates (Fig. 7) indicate that no major fractionation occurred during precipitation of calcite, and that the REY composition of the fluid was mainly controlled by local fluid-rock interaction. High concentrations and well-preserved Ce and Y anomalies suggest an increase in fluid-rock interactions (veins P21 and P20b). Low REY concentrations and less preserved Ce and Y anomalies suggest that interaction between meteoric water and host-rock limestone was limited, possibly due to fast descending and/or circulation of fluids transported by advection within opening-mode fractures. Previous studies of fault-related calcite veins and cements within the DSFZ also suggest formation by meteoric fluids, interacting with carbonate host-rocks to various degrees (Janssen et al., 2007).

7.2. Vein growth mechanism

The microstructures of the Kefar Giladi calcite-filled veins are mostly elongated-blocky to fibrous, indicating crystallographically

continuous overgrowths at the tips of existing grains. However, during the long history of vein growth, hiatuses readily occurred, forming euhedral and truncated faces termination zones parallel to vein walls (Fig. 5c–h). Kinematic and experimental based models for crystal growth under crack-seal mechanism indicate that crystals lose their facets morphology if the space available is sealed prior to the occurrence of the next cracking event (Urai et al., 1991; Hilgers et al., 2004). The abundance of sharp termination zones with truncated crystal faces in the Kefar Giladi veins (Table 1) indicates that the average rate of calcite crystal growth was higher than the average dilation rate of the corresponding fractures, and that vein growth mechanism involved episodes of fracturing and sealing (or partial sealing).

It is possible that the lack of direct evidence for the 'crack-seal' mechanism [i.e., fluid inclusions and dust trails with spacing on the order of 10 μm; (Ramsay, 1980)] is due to the relative large-scale of incremental opening. The spacing of truncated hiatus zones in vein samples is on the order of 0.5–10 mm (Fig. 5d). With large opening increments (mm scale), the calcite crystals effectively grow into a free space, where the only interference is between the growing crystals. This mechanism produces blocky and elongated-blocky textures and occasionally growth competition textures between grains (Fig. 5a). With time, however, opening-mode fractures are constrained by calcite growth, which are then associated with elongated-blocky and fibrous textures. It is generally agreed that fibrous or elongated columnar fabrics form by slow opening by aseismic crack-sealing mechanism (e.g. Gratier and Gamond, 1990). Thus, following a vein reopening event, calcite grains may either continue their growth at the tip of existing grains (e.g. P14; Fig. 5d), or nucleate and produce growth competition texture (e.g. P14; Fig. 5g) within the opening-mode fracture.

A schematic representation of the episodic vein growth is shown in Fig. 9. It shows the host rock of Bar Kokhba limestone prior to vein initiation (Fig. 9a), which is fractured or reactivated in response to N–S extension, giving rise to the formation of a dilation breccia (Fig. 9b). Subsequent to fracture opening, meteoric water enriched with carbonic acid percolates in the subsurface, leaching calcium carbonate from the host-rock limestone, and precipitating calcite minerals in an opening-mode fracture (Fig. 9c). Due to fast growth of calcite minerals relative to vein opening, sealing or partial sealing of the fracture occurs. Calcite minerals terminate against "opposing walls", forming truncated hiatuses morphology (Fig. 9d). The formation of successive parallel sealing-hiatuses, such as those observed in sample P14 (Fig. 5d), may occur due to small-scale opening episodes and subsequent calcite filling by continuous overgrowth at the tip of existing grains (Fig. 9e). Following larger-scale opening episodes (Fig. 9f), calcite may nucleate and develop free growth textures in the opening-mode fracture.

7.3. Vein initiation and termination ages

The microstructural results indicate that vein development was episodic rather than continuous, and that episodes of dilation were followed by calcite precipitation. Thus, U–Th ages of calcite-filled veins could correspond to the timing of vein initiation and/or reopening events of fractures in the subsurface.

The transition from vein walls inward into the calcite vein fill preserves information on the relative timing of initial fracture opening and vein growth by calcite precipitation into the open fracture. In most of the studied veins, the transition from breccia zone to calcite vein-fill appears to be sharp (Fig. 4). Type-1 breccias formed before the initial opening of the fracture as evident by the presence of sharp cutting edges and fragments that are aligned parallel to vein walls (Fig. 4a). Type-2 dilation breccias postdate the type-1 breccias and have coarsely crystalline calcite cements (Fig. 4c) that grew into open voids. The incorporation of vein-wall fragments, coated with thin calcite layer, into the breccia zone, as observed in vein P26 (Fig. 3d), suggests that further dilation occurred following vein initiation and calcite precipitation. This observation suggests that brecciation and dilation were associated with precipitation of calcite as breccia cement and as vein-fill. However, resealing the voids with the coarsely crystalline calcite cement likely occurred during a longer time period compared with the rapid events of fracture dilation. Thus, type-2 breccias are suggested to form during and following fracture dilation.

The oldest U–Th ages for calcite breccia-cement (P20 and P11) and calcite vein fill (samples P11, P20 and P21) are at the limit of U–Th method (>500; Table 1), and therefore accurate age constraints on the timing of vein initiation is not possible. The ages of initiation and/or reactivation for the other veins are clustered in four main growth periods. These periods are: 350–360 ka (initiation of veins P10 and P14), 250–280 ka (initiation of vein P12 and reopening of veins P20 and P21), 155 ka (initiation of vein P15), and 38–17 ka (reopening and growth of veins P20, P21, P14, P15 and P12). The combined results of calcite breccia cement and calcite vein fill indicate that some veins initiated prior to 500 ka. This is in agreement with the U–Th results of a similar study of calcite-filled veins from the nearby Har-Zefiyya fault (Fig. 1b; Nuriel et al., 2011). However, the majority of the veins in the Kefar Giladi quarry indicate that vein dilation and development were enhanced during the period between 358 and 17 ka.

The youngest obtained U–Th ages range between 38 and 17 ka (Fig. 8). During most of the late-Pleistocene, precipitation was not the limiting factor for vein growth as evident by the formation of nearby speleothems at the latitude of the study area (Bar-Matthews et al., 2003). Noteworthy, most of the samples are sealed veins with limited or no available space for growth (Fig. 3d, f and 5c). Therefore vein termination during the period between 38 and 17 ka (Fig. 8) is likely to reflect changes in the deformation regime, whereby

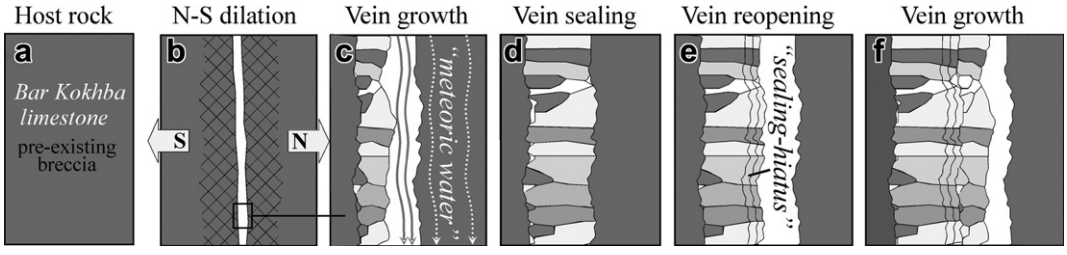

Fig. 9. Schematic model for the formation and growth history of calcite-filled veins. (a) host rock prior to vein initiation; (b) formation of dilation breccias, followed by initial fracturing due to N–S extension; (c) precipitation of calcite minerals in an opening-mode fracture; (d) sealing or partial sealing of the fracture by calcite minerals terminating against an "opposing wall"; (e) formation of successive parallel sealing-hiatuses prior to major reopening episode; (f) major vein reopening followed by calcite deposition in the opening-mode fracture [crystal shape and growth texture are modified after Bons (2000) based on simulation of vein growth into an open cavity].

dilation is suppressed and fracture are sealed by vein-fill material rather than due to changes in environmental conditions (e.g. fluids, pCO_2).

7.4. Formation of opening-mode fractures in a convergent strike-slip setting

The calcite-filled veins were emplaced within a contractional block in between two major segments of the DSFZ (Weinberger et al., 2009). Weinberger and Sneh (2004) and Weinberger et al. (2009) calculated ~E–W localized shortening of up to 30%, which resulted in a topographic rise due to folding of at least ~80 m in the last 1 Ma (Weinberger et al., 2011). We suggest that this E–W shortening gave rise to an orthogonal ~N–S extension under pure shear conditions. The imposed extensional strain was released by the brittle processes of brecciation and dilation, giving rise to the formation of ~E–W striking opening-mode fractures and the dilation of some ~NW–SE striking subsidiary faults. These pre-existing faults formed during the early phase of deformation (e.g. NW–SE shortening; see section 2), but selectively dilated in the late phase of deformation. This explains the scattering in vein directions with a dominant ~E-W striking set and a second, less prominent, ~NW–SE striking set (Fig. 2c). Based on the initial timing of fracturing (~358 ka) and the estimated erosion rates in the area [<0.05 m/ka; Begin and Zilberman (1997)], we can estimate the overburden at the time of fracturing as less than 100 m.

Gomez et al. (2007) proposed a two-stage evolution of the Lebanese restraining bend (LRB in Fig. 1a): an early phase of Miocene to Pliocene deformation involving strike-slip motion and block rotation, and a later, currently active phase of deformation involving strain partitioning. They attributed this tectonic transition to an increasing plate convergence between the Sinai sub-plate and the Arabian plate. Based on geological observations, Weinberger et al. (2009) have also proposed a transition from an early (Miocene-Pliocene) phase of pure strike-slip motion to a late (Pleistocene) phase of convergent strike slip of "partitioned" transpression. The latter is characterised by discrete left-lateral strike-slip motion across weak N–S striking faults and the development of N–S trending folds and reverse faults in the intervening blocks in response to shortening perpendicular to the transform boundary (Weinberger et al., 2009; Levi and Weinberger, 2011). The ~E–W calcite-filled veins are another manifestation of this strain partitioning, and their association with the late phase of convergent strike-slip motion helps to constrain the timing of this tectonic transition. The deformed ~1 Ma Hazbani basalt provides a maximum age for the tectonic transition (Weinberger et al., 2009), whereas the timing of enhanced vein development, between 358 and 17 ka, provides a minimum age for this transition. It is likely that vein formation lagged somewhat after the initial formation of the ~N–S trending folds and reverse faults, but may represent the timing of increasing plate convergence along this sector of the DSFZ.

8. Conclusions

Based on field observations, microstructural investigations, geochemical data and geochronological constraints, the following conclusions can be drawn:

1) Stable isotope and REY results indicate that calcite vein fill precipitated from meteoric water enriched by C_3-type Mediterranean vegetation and under low (5–30 °C) temperature conditions. The composition of the fluids was mainly controlled by local fluid-rock interactions with no evidence for input of deep-seated or exotic fluids.
2) Brecciation and dilation were associated with the precipitation of coarsely crystalline calcite cement and calcite bands close to the vein walls. Large opening increments (mm scale) allowed calcite crystals to grow effectively into a free space, producing elongated-blocky textures with occasional growth competition textures. Nevertheless, the abundance of hiatuses in most veins indicates that sealing and reopening episodes were important factors in the vein growth mechanism.
3) U–Th ages correspond to the time of growth episode associated with major opening events. The oldest ages indicate that some vein initiation occurred prior to 500 ka. The majority of the veins in this study initiated and developed during the period between 358 and 17 ka. Most veins are currently sealed structures, with youngest obtained U–Th ages ranging between 38 and 17 ka, indicating that calcite growth exceeded dilation processes.
4) Calcite-filled veins were emplaced within a tectonically deformed contractional block of the DSFZ. The formation of ~E–W calcite-filled veins is a manifestation of "partitioned" transpression. The results indicate that this partitioned transpression, associated with increasing plate convergence along this sector of the DSFZ, took place between 358 and 17 ka.

Acknowledgements

We wish to thank Dr Yuexing Feng for providing technical help with TIMS U-Th analyses and Dr Wan-Ping (Sunny) Hu for her assistance with ICP-Ms analyses. Ms Kim Baublys is thanked for her kind assistance with stable isotope mass spectrometry. RW and MG were supported by grant 2004232 from the United States – Israel Binational Scientific Foundation. Thorough and constructive reviews by Anne-Marie Boullier and an anonymous reviewer greatly improved this paper.

Appendix. Supplementary material

Supplementary data associated with this article can be found, in the online version, at doi:10.1016/j.jsg.2011.12.010.

References

Bar-Matthews, M., Ayalon, A., Matthews, A., Sass, E., Halicz, L., 1996. Carbon and oxygen isotope study of the active water-carbonate system in a karstic Mediterranean cave: implications for paleoclimate research in semiarid regions. Geochimica et Cosmochimica Acta 60 (2), 337–347.

Bar-Matthews, M., Ayalon, A., Gilmour, M., Matthews, A., Hawkesworth, C.J., 2003. Sea - land oxygen isotopic relationships from planktonic foraminifera and speleothems in the Eastern Mediterranean region and their implication for paleorainfall during interglacial intervals. Geochimica et Cosmochimica Acta 67 (17), 3181–3199.

Bau, M., Dulski, P., 1999. Comparing yttrium and rare earths in hydrothermal fluids from the Mid-Atlantic Ridge: implications for Y and REE behaviour during near-vent mixing and for the Y/Ho ratio of proterozoic seawater. Chemical Geology 155 (1–2), 77–90.

Begin, Z.B., Zilberman, E., 1997. Main Stages and Rate of Relief Development in Israel Geological Survey of Israel Report GSI/24/97, 63 (in Hebrew, English abstract).

Berger, B.R., 2007. The 3D Fault and Vein Architecture of Strike-Slip Releasing- and Restraining Bends: Evidence from Volcanic-Centre-Related mineral Deposits. In: Geological Society Special Publication, vol. 290, pp. 447–471.

Boles, J.R., Eichhubl, P., Garven, G., Chen, J., 2004. Evolution of a hydrocarbon migration pathway along basin-bounding faults; evidence from fault cement. American Association of Petroleum Geologists Bulletin 88 (7), 947–970.

Bolhar, R., Kamber, B.S., Moorbath, S., Fedo, C.M., Whitehouse, M.J., 2004. Characterisation of early Archaean chemical sediments by trace element signatures. Earth and Planetary Science Letters 222 (1), 43–60.

Bons, P.D., 2000. The formation of veins and their microstructures. In: Jessell, M.W., Urai, J.L. (Eds.), Stress, Strain and Structure, a Volume in Honour of W D Means. Journal of the Virtual Explorer, vol. 2, p. 12.

Bons, P.D., 2001. Development of crystal morphology during unitaxial growth in a progressively widening vein: I. The numerical model. Journal of Structural Geology 23 (6–7), 865–872.

Boullier, A.-M., Fujimoto, K., Ohtani, T., Roman-Ross, G., Lewin, E., Ito, H., Pezard, P., Ildefonse, B., 2004. Textural evidence for recent co-seismic circulation of fluids in the Nojima fault zone, Awaji island, Japan. Tectonophysics 378 (3–4), 165–181.

Bourne, S.J., Willemse, E.J.M., 2001. Elastic stress control on the pattern of tensile fracturing around a small fault network at Nash Point, UK. Journal of Structural Geology 23 (11), 1753–1770.

Cheng, H., Edwards, R.L., Hoff, J., Gallup, C.D., Richards, D.A., Asmerom, Y., 2000. The half-lives of uranium-234 and thorium-230. Chemical Geology 169 (1–2), 17–33.

Cox, S.F., 2007. Structural and isotopic constraints on fluid flow regimes and fluid pathways during upper crustal deformation: an example from the Taemas area of the Lachlan Orogen, SE Australia. Journal of Geophysical Research 112, B08208. doi:10.1029/2006JB004734.

De Paola, N., Holdsworth, R.E., Collettini, C., 2008. The internal structure of dilational stepovers in regional transtension zones. International Geology Review 50 (3), 291–304.

Durney, D.W., Ramsay, J.G., 1973. Incremental strains measured by syntectonic crystal growths. In: De Jong, K.A., Scholten, R. (Eds.), Gravity and Tectonics. Wiley, New York, pp. 67–96.

Eggins, S.M., Woodhead, J.D., Kinsley, L.P.J., Mortimer, G.E., Sylvester, P., McCulloch, M.T., Hergt, J.M., Handler, M.R., 1997. A simple method for the precise determination of ≥40 trace elements in geological samples by ICPMS using enriched isotope internal standardisation. Chemical Geology 134 (4), 311–326.

Eichhubl, P., Davatzes, N.C., Becker, S.P., 2009. Structural and diagenetic control of fluid migration and cementation along the Moab fault, Utah. American Association of Petroleum Geologists Bulletin 93 (5), 653–681.

Eyal, M., Eyal, Y., Bartov, Y., Steinitz, G., 1981. The tectonic development of the western margin of the Gulf of Elat (Aqaba) rift. Tectonophysics 80 (1–4), 39–66.

Faleiros, F.M., Campanha, G.A.d.C., Bello, R.M.d.S., Fuzikawa, K., 2007. Fault-valve action and vein development during strike-slip faulting: an example from the Ribeira Shear Zone, Southeastern Brazil. Tectonophysics 438 (1–4), 1–32.

Fisher, D.M., Brantley, S.L., Everett, M., Dzvonik, J., 1995. Cyclic fluid flow through a regionally extensive fracture network within the Kodiak accretionary prism. Journal of Geophysical Research 100 (B7), 12881–12894.

Fleet, A.J., 1984. Aqueous and sedimentary geochemistry of the rare earth elements (REE). In: Henderson, P. (Ed.), Rare Earth Element Geochemistry. Developments in Geochemistry, vol. 2. Elsevier, pp. 343–373.

Freund, R., Zak, I., Garfunkel, Z., 1968. Age and rate of the sinistral movement along the Dead Sea Rift. Nature 220 (5164), 253–255.

Garfunkel, Z., 1981. Internal structure of the Dead Sea leaky transform (rift) in relation to plate kinematics. Tectonophysics 80 (1–4), 81–108.

Gomez, F., Karam, G., Khawlie, M., McClusky, S., Vernant, P., Reilinger, R., Jaafar, R., Tabet, C., Khair, K., Barazangi, M., 2007. Global positioning system measurements of strain accumulation and slip transfer through the restraining bend along the Dead Sea fault system in Lebanon. Geophysical Journal International 168 (3), 1021–1028.

Gratier, J.P., Gamond, J.F., 1990. Transition between seismic and aseismic deformation in the upper crust. In: Knipe, R.J., Rutter, E.H. (Eds.), Deformation Mechanisms, Rheology and Tectonics. Geological Society Special Publication, vol. 54, pp. 461–473.

Gross, M.R., Engelder, T., 1995. Strain accommodated by brittle failure in adjacent units of the Monterey Formation, USA: scale effects and evidence for uniform displacement boundary conditions. Journal of Structural Geology 17 (9), 1303–1318.

Gross, M.R., Gutiérrez-Alonso, G., Bai, T., Wacker, M.A., Collinsworth, K.B., Behl, R.J., 1997. Influence of mechanical stratigraphy and kinematics on fault scaling relations. Journal of Structural Geology 19, 171–183.

Hancock, P.L., 1985. Brittle microtectonics: principles and practice. Journal of Structural Geology 7 (3–4), 437–457.

Haskin, L.A., Helmke, P.A., Paster, T.P., Allen, R.O., 1971. Rare earths in meteoritic, terrestrial, and lunar matter. In: Brunfelt, A., Steinnes, E. (Eds.), Activation Analysis in Geochemistry and Cosmochemistry. Universitetsforlaget, Oslo, pp. 201–218.

Heimann, A., 1990. The Development of the Dead Sea Rift and Its Margins in Northern Israel during the Pliocene and the Pleistocene Geological Survey of Israel Report GSI 28/90, 76.

Hempton, M.R., 1987. Constraints on Arabian plate motion and extensional history of the Red Sea. Tectonics 6, 687–705.

Hilgers, C., Urai, J.L., 2002. Microstructural observations on natural syntectonic fibrous veins: implications for the growth process. Tectonophysics 352 (3–4), 257–274.

Hilgers, C., Dilg-Gruschinski, K., Urai, J.L., 2004. Microstructural evolution of syntaxial veins formed by advective flow. Geology 32 (3), 261–264.

Janssen, C., Romer, R.L., Hoffmann-Rothe, A., Mingram, B., Dulski, P., Möller, P., Al-Zubi, H., 2005. The role of fluids in faulting deformation: a case study from the Dead Sea Transform (Jordan). International Journal of Earth Sciences 94 (2), 243–255.

Janssen, C., Romer, R.L., Plessen, B., Naumann, R., Hoffmann-Rothe, A., Matar, A., 2007. Contrasting fluid regimes along the dead Sea transform. Geofluids 7 (3), 275–291.

Joffe, S., Garfunkel, Z., 1987. Plate kinematics of the circum Red Sea - a re-evaluation. Tectonophysics 141 (1–3), 5–22.

Ku, T.-L., 1965. An evaluation of the U^{234}/U^{238} method as a tool for dating pelagic sediments. Journal of Geophysical Research 70 (14), 3457–3474.

Lawrence, M.G., Kamber, B.S., 2006. The behaviour of the rare earth elements during estuarine mixing-revisited. Marine Chemistry 100 (1–2), 147–161.

Levi, T., Weinberger, R., 2011. Magnetic fabrics of diamagnetic rocks and the strain field associated with the Dead Sea Fault, northern Israel. Journal of Structural Geology 33, 566–578.

Ludwig, K.R., 1991. ISOPLOT: A Plotting and Regression Program for Radiogenic-Isotope Data; Version 2.2. United States Geological Survey. Open-File Report, 42.

McGarry, S., Bar-Matthews, M., Matthews, A., Vaks, A., Schilman, B., Ayalon, A., 2004. Constraints on hydrological and paleotemperature variations in the Eastern Mediterranean region in the last 140 ka given by the δD values of speleothem fluid inclusions. Quaternary Science Reviews 23 (7–8), 919–934.

Meghraoui, M., Gomez, F., Sbeinati, R., Van der Woerd, J., Mouty, M., Darkal, A.N., Radwan, Y., Layyous, I., Al Najjar, H., Darawcheh, R., Hijazi, F., Al-Ghazzi, R., Barazangi, M., 2003. Evidence for 830 years of seismic quiescence from palaeoseismology, archaeoseismology and historical seismicity along the Dead Sea fault in Syria. Earth and Planetary Science Letters 210 (1–2), 35–52.

Mor, D., 1993. A time-table for the levant volcanic province, according to K-Ar dating in the golan heights, Israel. Journal of African Earth Sciences 16 (3), 223–234.

Niemi, T.M., Zhang, H., Atallah, M., Harrison, J.B.J., 2001. Late Pleistocene and Holocen slip rate of the northern Wade Araba fault, dead Sea transform, Jordan. Journal of Seismology 5 (3), 449–474.

Nuriel, P., Rosenbaum, G., Uysal, I.T., Zhao, J.-x., Golding, S.D., Weinberger, R., Karabacak, V., Avni, Y., 2011. Formation of Fault-Related Calcite Precipitates and Their Implications for Dating Fault Activity in the East Anatolian and Dead Sea Fault Zones. In: Geological Society of London, Special Publication in Honors of Rick Sibson, 359 (1), 229–248.

O'Neil, J.R., Clayton, R.N., Mayeda, T.K., 1969. Oxygen isotope fractionation in divalent metal carbonates. Journal of Chemical Physics 51 (12), 5547–5558.

Peacock, D.C.P., 2001. The temporal relationship between joints and faults. Journal of Structural Geology 23 (2–3), 329–341.

Quennell, A.M., 1958. The structural and geomorphologic evolution of the Dead Sea Rift. Journal of Geological Society of London 114, 1–24.

Ramsay, J.G., 1980. The crack-seal mechanism of rock deformation. Nature 284 (5752), 135–139.

Richards, D.A., Dorale, J.A., 2003. Uranium-series Chronology and Environmental Applications of Speleothems. Reviews in Mineralogy and Geochemistry. Mineralogical Society of America and Geochemical Society, Washington, DC, United States, pp. 407–460.

Sample, J.C., 2010. Stable isotope constraints on vein formation and fluid evolution along a recent thrust fault in the Cascadia accretionary wedge. Earth and Planetary Science Letters 293 (3–4), 300–312.

Sibson, R.H., 1985. Stopping of earthquake ruptures at dilational fault jogs. Nature 316 (6025), 248–251.

Sibson, R.H., 1987. Earthquake rupturing as a mineralizing agent in hydrothermal systems. Geology 15 (8), 701–704.

Sneh, A., Weinberger, R., 2003. Geology of the Metulla quadrangle, northern Israel: implications for the offset along the Dead Sea Rift. Israel Journal of Earth Sciences 52 (3–4), 123–138.

Steinitz, G., Bartov, Y., 1991. The Miocene-Pleistocene history of the Dead Sea segment of the Rift in the light of K-Ar of basalts. Israel Journal of Earth Sciences 40 (1–4), 199–208.

Swanson, M.T., 2006. Late Paleozoic strike-slip faults and related vein arrays of Cape Elizabeth, Maine. Journal of Structural Geology 28 (3), 456–473.

Swart, P.K., Burns, S.J., Leder, J.J., 1991. Fractionation of the stable isotopes of oxygen and carbon in carbon dioxide during the reaction of calcite with phosphoric acid as a function of temperature and technique. Chemical Geology 86 (2), 89–96.

Urai, J.L., Williams, P.F., van Roermund, H.L.M., 1991. Kinematics of crystal growth in syntectonic fibrous veins. Journal of Structural Geology 13 (7), 823–836.

Uysal, I.T., Feng, Y., Zhao, J.-x., Altunel, E., Weatherley, D., Karabacak, V., Cengiz, O., Golding, S.D., Lawrence, M.G., Collerson, K.D., 2007. U-series dating and geochemical tracing of late Quaternary travertine in co-seismic fissures. Earth and Planetary Science Letters 257 (3–4), 450–462.

Uysal, I.T., Feng, Y, Zhao, Işik, V., Nuriel, P., Golding, S.D., 2009. Hydrothermal CO_2 degassing in seismically active zones during the late Quaternary. Chemical Geology 265, 442–454.

Uysal, I.T., Feng, Y.-X., Zhao, J.-X., Bolhar, R., Isik, V., Baublys, K.A., Yago, A., Golding, S.D., 2011. Seismic cycles recorded in late Quaternary calcite veins: geochronological, geochemical and microstructural evidence. Earth and Planetary Science Letters 303 (1–2), 84–96.

Veizer, J., Hoefs, J., 1976. The nature of O^{18}/O^{16} and C^{13}/C^{12} secular trends in sedimentary carbonate rocks. Geochimica et Cosmochimica Acta 40 (11), 1387–1395.

Verhaert, G., Muchez, P., Sintubin, M., Similox-Tohon, D., Vandycke, S., Waelkens, M., 2003. Reconstruction of neotectonic activity using carbonate precipitates: a case study from the northwestern extremity of the Isparta Angle (SW Turkey). Journal of Geochemical Exploration 78-79, 197–201.

Verhaert, G., Muchez, P., Sintubin, M., Similox-Tohon, D., Vandycke, S., Keppens, E., Hodge, E.J., Richards, D.A., 2004. Origin of palaeofluids in a normal fault setting in the Aegean region. Geofluids 4 (4), 300–314.

Weinberger, R., Sneh, A., 2004. The Geology of Qiryat Shemona Region Israel Geological Society Annual Meeting, HaGoshrim, Field trips guidebook, 55–78 (in Hebrew).
Weinberger, R., Gross, M.R., Sneh, A., 2009. Evolving deformation along a transform plate boundary: example from the Dead Sea Fault in northern Israel. Tectonics 28. doi:10.1029/2008TC002316.
Weinberger, R., Schattner, U., Medvedev, B., Frieslander, U., Sneh, A., Harlavan, Y., Gross, R.M., 2011. Convergent strike-slip across the Dead Sea Fault in northern Israel imaged by high-resolution seismic reflection data. Israel Journal of Earth Sciences 58, 143–156. doi:10.1560/IJES.58.2–3.143.
Yu, K.-F., Zhao, J.-X., Shi, Q., Chen, T.-G., Wang, P.-X., Collerson, K.D., Liu, T.-S., 2006. U-series dating of dead Porites corals in the South China sea: evidence for episodic coral mortality over the past two centuries. Quaternary Geochronology 1 (2), 129–141.
Zhao, J.-x., Hu, K., Collerson, K.D., Xu, H., 2001. Thermal ionization mass spectrometry U-series dating of a hominid site near Nanjing, China. Geology 29 (1), 27–30.